

Improving Atmospheric River Forecast Over Himalayas using Convolutional Neural Network

Sheikh Imran Fayaz¹, Munir Ahmad Nayak², Adnan Kaisar Khan¹

¹sheikhimranfayaz@gmail.com, ²munir.nayak@nitsri.ac.in, ¹adnankaisarkhan@gmail.com

¹Department of Civil Engineering, National Institute of Technology Srinagar, India, ² Assistant Professor, Department of Civil Engineering, National Institute of Technology Srinagar, India

This manuscript is a non-peer-reviewed preprint submitted to EarthArXiv.

This preprint has also been submitted for peer review to:

International Journal of Climatology

The content of this manuscript is under review. The authors welcome comments and feedback from the research community.

Keywords

Atmospheric Rivers; Integrated Vapor Transport; Convolutional Neural Network; Numerical Weather Prediction; Himalayas; GFS; Deep Learning

Abstract

Extreme precipitation over the Himalayas is often linked to Atmospheric Rivers (ARs) interacting with its unique and complex topography. The topographic complexity and sparse observational data constitute a challenging problem for numerical weather prediction models. We find that the widely used Global Forecast System (GFS) exhibits systematic errors for high magnitude Integrated Vapor Transport (IVT), and its predicted AR structure and direction exhibits significant mismatches with observations. Our work proposes a modified convolutional neural network model, based on a previously-developed ARcnn, for IVT over South Asian including the Himalayas. ARcnn significantly improves the error metrics, root mean square error (RMSE), bias in high-IVT, and directional mean angular error (MAE), for both 24-hour lead and 7-day lead forecasts over the Himalayan region. The results in this study indicate the improved IVT forecast across the study entire area and more specifically over the Himalayas. Further, the ARcnn model was able to correct IVT that made it possible to detect the ARs missed in GFS forecasts for both lead times. Thus, these results provide compelling evidence of ARcnn's powerful postprocessing capability and its potential for using in early prediction tools for IVT and AR.

30 1. Introduction

31 Coherent lower tropospheric structures of large moisture flux flows with length exceeding 2000
32 km and maximum width of 1000 km are known as Atmospheric Rivers (ARs). These form a major
33 contributor to poleward moisture transport across the midlatitude and synoptic scale moisture
34 circulation (Zhu & Newell, 1998; Guan & Waliser, 2019). ARs have a strong influence over the
35 precipitation trends and alleviating the droughts, but also pose a danger to flooding and landslides
36 (Payne et al., 2020). Over the western coast United States, the mean annual precipitation by ARs
37 is about 30–65%. Also, in the west coast of North America more than 60% of extreme
38 hydrometeorological events are linked to ARs (Lamjiri et al., 2017 ;Gershunov et al., 2017). In
39 spite of the low occurrence of the ARs, these contribute about one-third of annual snow
40 accumulation (Guan et al., 2010). Asia-Pacific region ARs cause rainfall of about 50–60 mm day⁻¹
41 with their intensities reaching to nearly 80 mm day⁻¹ when interacting with terrain, and achieve
42 the maximum value when coexisting with tropical cyclones (Wu et al., 2026). These findings
43 highlight the importance of ARs for water management. Since the strength and associated impacts
44 of ARs are strongly linked with Integrated Vapor Transport (IVT), metric for AR identification
45 and quantification. Thus the reliable representation of IVT is fundamental for predicting extreme
46 precipitation, flooding risk, and related hydrological hazards (Ralph et al., 2018).

47 ARs display a distinct effect over the Himalayan Mountains, where the extreme topography and
48 highly sensitive climate augment the hydrological impacts. The relatively low occurrence of ARs
49 in the Himalayas compared to coastal regions does not reduce their impacts due to the region's
50 steep terrain. This intense effect is characterized by a significant increase in moisture transport and
51 rising freezing levels, that drives a critical transition from snow to rain, which reduces frozen
52 precipitation and destabilizes snowpack (Nayak et al. 2021). The elevated freezing levels increase
53 the liquid runoff and rainfall on snow that increase the glacier melt and alters the mass balance of
54 major river basins like the Brahmaputra, Indus, and Ganges. The Orographic lifting of ARs
55 frequently triggers localized heavy rainfall strongly associated with extreme landfall flooding in
56 India (Mahto et al. 2023). The variations caused to the hydrological cycle from ARs escalate the
57 risk of flash floods and landslides, posing a threat to safety and water security to the vulnerable
58 downstream communities.

59 The widely used Numerical Weather Prediction (NWP) model is the Global Forecast System
60 (GFS). It is used to predict IVT, but the issue is that it exhibits systematic errors in IVT magnitude
61 and spatial structure. The challenge faced by the GFS is that it struggles to accurately forecast

62 high-magnitude IVT during strong moisture transport events (Chapman et al., 2019). GFS IVT
63 predictions also show frequent spatial displacement of IVT plumes, which is responsible for errors
64 in AR landfall location that reduces the forecast skill for heavy precipitation and floods (Wick et
65 al., 2013). Beyond the IVT magnitude and position, the orientation of AR i.e. IVT direction also
66 plays a significant role in precipitation and determines the rainfall patterns related to the AR.
67 Research shows that two different catchments, Teifi and Dyfi in UK, produce high precipitation
68 for different AR orientation. This is because if the orientation of the AR is more orthogonal to the
69 terrain, it will cause high precipitation whereas if it has a more oblique orientation, precipitation
70 response will be weak (Hecht et al. 2017; Griffith et al. 2020). But the zonal (U) and meridional
71 (V) wind components of GFS forecasts (Guo et al., 2024) used directly in IVT calculations also
72 shows errors that will be propagated in the moisture transport estimates and will finally affect the
73 AR orientation and associated rainfall. On a broader perspective, the GFS provides reliable IVT
74 predictions, but it continues to exhibit significant errors in IVT magnitude, position, and wind-
75 related components of moisture transport, especially during AR events.

76 Convolutional Neural Network (CNN) is a deep learning framework that recognizes hierarchical
77 features in a grided image to perform classification or regression tasks. Core components of CNN
78 consist mainly of three stages as briefly stated. Convolutional layers which use kernels, 2D learned
79 weight matrices, to extract features from gridded image data. Pooling Layers summarize the
80 features generated to provide distortion invariance. Lastly, the fully connected layers map the final
81 features generated to a final output for a classification task like in healthcare and autonomous
82 systems. This is the structure of early CNN's used for classification, but as research on computer
83 vision progressed, CNNs have been used for regression tasks as well. The "Half-CNN" framework
84 demonstrated that by removing fully connected layers, an image regression CNN model is
85 achieved (Yuan et al. 2014). This framework makes CNN ideal for spatial prediction regression
86 tasks. Thus, this work adopts a CNN deep learning model for GFS IVT fields post processing to
87 improve IVT maps for better AR prediction over the Himalayan region.

88 Deep learning (DL) has emerged as a reliable algorithm for weather forecasting for short- term
89 leads and AR forecast improvement (Bi, K et al.; Chen, L. et al.; Tian, Y. et al.; Singh, S. et al.).
90 .Most notably, Chapman et al. (2019) introduced a ML CNN model for postprocessing GFS IVT
91 forecasts and demonstrated substantial improvements in IVT magnitude and moisture-transport
92 pathways. However, this effort was focused for the western United States and Eastern Pacific
93 regions. No such ML AR-postprocessing model has been developed and trained for the Himalayas.
94 This highlights the need for a region-specific Himalayan ML model.

95 Accordingly, the objective of this research is to adapt a CNN-based deep learning framework
96 specifically trained for the region with the Himalayan domain. While existing deep learning
97 models for post-processing IVT and AR data have demonstrated high performance in Western
98 mid-latitude regions, their applicability to the high-altitude complex terrain of South Asia remains
99 limited. As the pre-defined models are trained on the specific regions and also do not correct the
100 direction component, this creates a modelling gap for our region of interest, which is distinct in
101 orographic uplift and AR characteristics, which thus needs to be filled for the Himalayan and the
102 adjoining region. Our developed CNN model fills this gap by modifying the existing model
103 according to the region's inherent complexities and also corrects the direction of IVT, so that a
104 robust region-specific CNN architecture is achieved to process the GFS IVT for accurate IVT and
105 AR prediction.

106 2. Data

107 This work utilizes two primary datasets: the Modern-Era Retrospective Analysis for Research and
108 Applications, Version 2 (MERRA-2) and GFS. For the purposes of model training, validation, and
109 testing the MERRA-2 reanalysis serves as the observational proxy for the ground truth, while GFS
110 IVT forecast fields constitute the input required to be corrected. The time range of data is from 17
111 January 2015 to 30 April 2025, for the extended cold season (October to April). Variables required
112 for computing IVT (specific humidity and wind components) were extracted for pressure levels of
113 1000 hpa to 300 hpa (McCarty et al., 2016; Gelaro et al., 2017). The spatial grid for which data is
114 used extends from 0°N to 40°N latitude and 50°E to 100°E longitude, providing a sufficient buffer
115 region for ARs interacting with Himalayan region.

116 2.1 GFS Forecast Data

117 GFS is an NWP model developed by the National Oceanic and Atmospheric Administration
118 (NOAA) branch of the National Centers for Environmental Prediction (NCEP). GFS operates daily
119 4 times at 0000, 0600, 1200, and 1800 UTC, and provides up to a 16-day forecast (Environmental
120 Modeling Center [EMC], 2016). It forecasts a wide range of atmospheric variables at various
121 spatial and temporal resolutions. The GFS IVT data is extracted from the NCEP GFS Global
122 Forecast Grids Historical Archive at a spatial resolution of $0.25^\circ \times 0.25^\circ$ (UCAR Research Data
123 Archive [RDA], 2024). GFS forecasts are available at 3-hour intervals for lead times up to 240
124 hours (10 days) and 12-hour intervals from 240 to 384 hours (10–16 days), thus providing both

125 short-term and long-term forecasts. This work initialized the GFS forecast at 0000 UTC with 24-
126 hour and 7-day lead times.

127 2.2 MERRA-2 Data

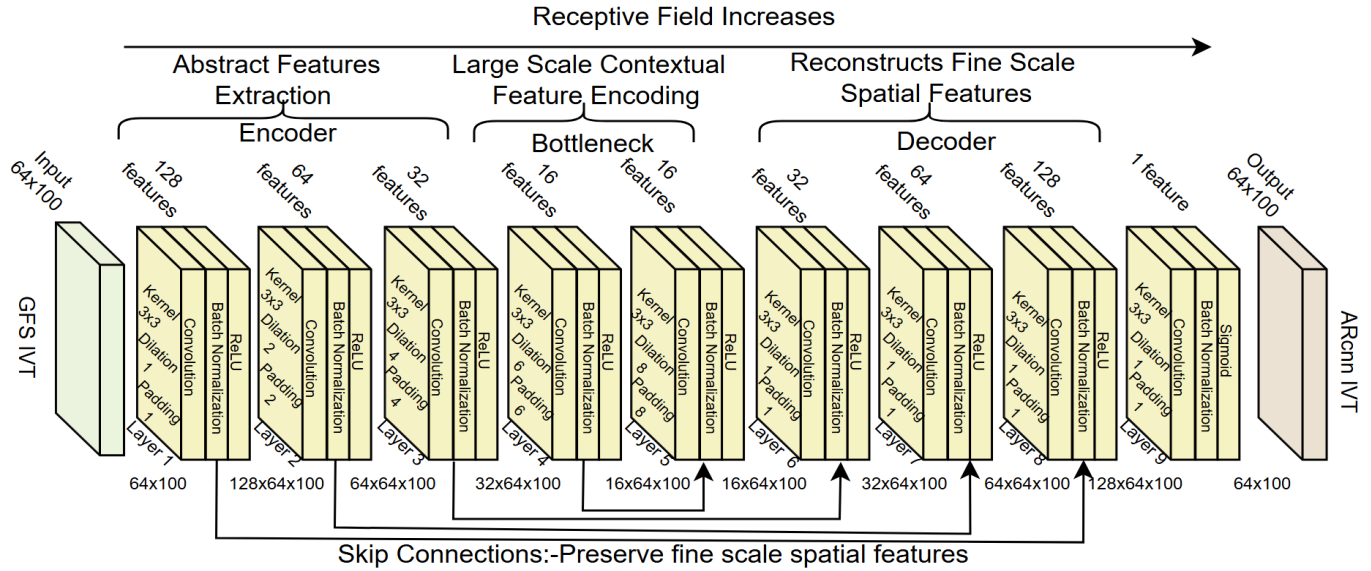
128 The NASA, Global Modelling and Assimilation Office (GMAO) developed a modern, high-quality
129 atmospheric reanalysis product known as Modern-Era Retrospective Analysis for Research and
130 Applications, Version 2 (MERRA-2). It incorporates a diverse collection of satellite and ground-
131 based data points using the GEOS-5 data assimilation system, providing temporally consistent
132 fields of atmospheric, land, and oceanic variables from 1980 onward (Gelaro et al., 2017). The
133 MERRA-2 dataset used in this study, with a spatial resolution of $0.625^\circ \times 0.5^\circ$, was downloaded
134 from NASA's Goddard Earth Sciences Data and Information Services Center (GES DISC) and
135 utilized for the computation of IVT. To ensure spatial alignment between the MERRA-2 and GFS
136 datasets, the GFS data (spatial resolution: $0.25^\circ \times 0.25^\circ$) was regridded to the MERRA-2 grid
137 resolution using the second-order conservative remapping method. This method conserves integral
138 quantities such as fluxes and minimizes spatial interpolation errors, which permits a reliable
139 comparison between forecasted and reanalysis-derived IVT fields

140 3. Method

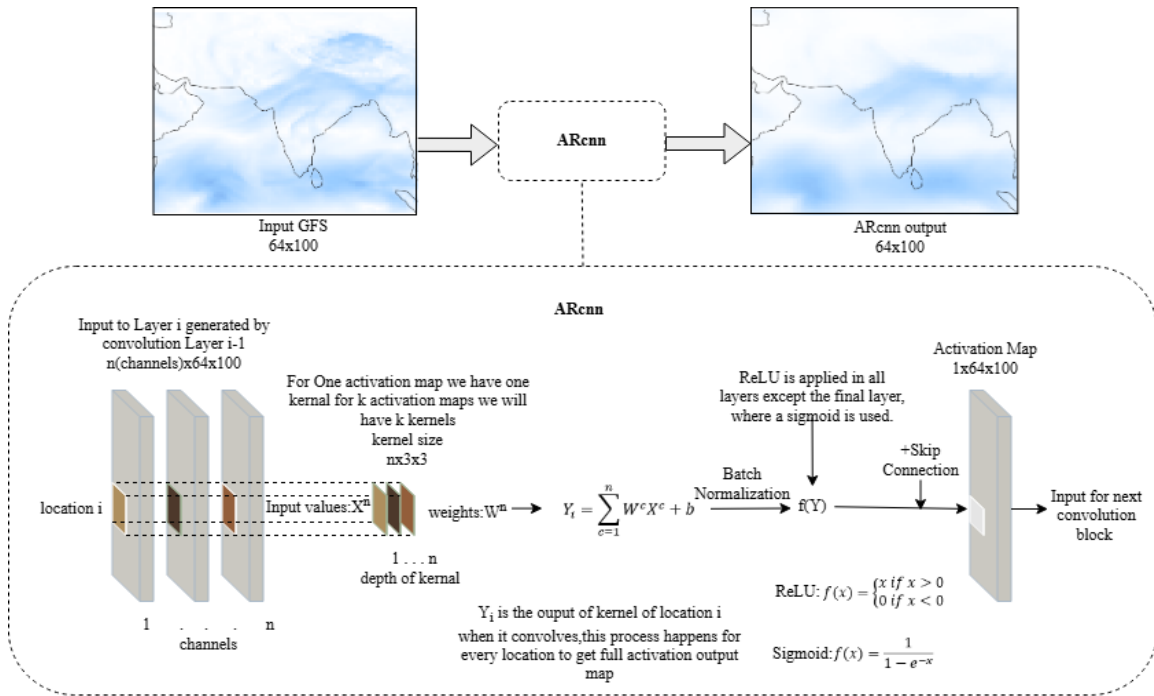
141 IVT consists of two components: magnitude and direction. The former represents the strength of
142 IVT plumes, and the latter represents the orientation of moisture fluxes. For correcting the biases
143 in both components, we develop two CNN models, collectively referred to as the ARcnn model.
144 The first model, named the ARcnn magnitude model, corrects the magnitude of IVT fields, while
145 the second model, referred to as the ARcnn direction model, corrects the IVT direction vectors.
146 The outputs from both models were combined, the magnitude field and the direction field, to obtain
147 bias-corrected IVT fields with improved prediction of intensity and direction of IVT plumes. The
148 Architecture of ARcnn Model is depicted in Figure 1 and Figure 2, for detailed discussion of the
149 model refer to supplementary Text S1 and S2.

150 For developing the ARcnn model framework, the dataset was divided into training, validation, and
151 testing subsets chronologically, following an 85:5:10 split, respectively. The training, validation,
152 and testing datasets range from 17 January 2015 to 29 December 2023, 30 December 2023 to 17
153 April 2024, and 18 April 2024 to 30 April 2025, respectively. The ARcnn model is trained
154 separately for 24 hour and 7-day lead times. For each lead time, the GFS and MERRA-2 IVT fields
155 are paired such that each GFS forecast with a lead time corresponds to the same-date MERRA-2

156 IVT field, forming valid input–target pairs for model training. After the model training for two
 157 different lead times, we will obtain two different sets of weights: one for 24 hour lead and the other
 158 for 7-day lead forecasts.



159
 160 Figure1. Architecture of ARcnn architecture showing details of features,dialtion,padding,kernel in each layer and skip connections



161
 162 Figure 2. layer-wise operations of the ARcnn model for a single convolutional kernel, resulting in one activation (output feature)
 163 map. This same process is repeated independently for each kernel in the layer, such that the total number of activation maps
 164 produced equals the number of output channels of that layer.

165 3.1 Metrics Used for Model Evaluation

166 For the test period, 24-h and 7-day lead GFS IVT forecasts were evaluated against the
167 corresponding MERRA-2 IVT fields, which serve as the reference dataset. The performance of the
168 ARcnn IVT magnitude model and GFS model IVT forecasts was quantified using four widely
169 adopted statistical metrics: Root Mean Square Error (RMSE), Centered Root Mean Square Error
170 (CRMSE), Bias, and Pearson Correlation (PC). Afterwards, the metrics were eventually used to
171 quantify the percentage improvement achieved by the ARcnn postprocessing with respect to the
172 baseline GFS forecasts.

173 The performance of the ARcnn IVT direction model and GFS IVT direction fields was assessed
174 using the Mean Angular Error (MAE), which measures the average angular difference between the
175 predicted (ARcnn or GFS IVT directions) and reference IVT direction vectors (MERRA-2 IVT
176 directions). This metric directly evaluates the accuracy of directional correction independent of
177 IVT magnitude and provides a physically meaningful assessment of improvements in moisture
178 transport orientation.

179 4. Results

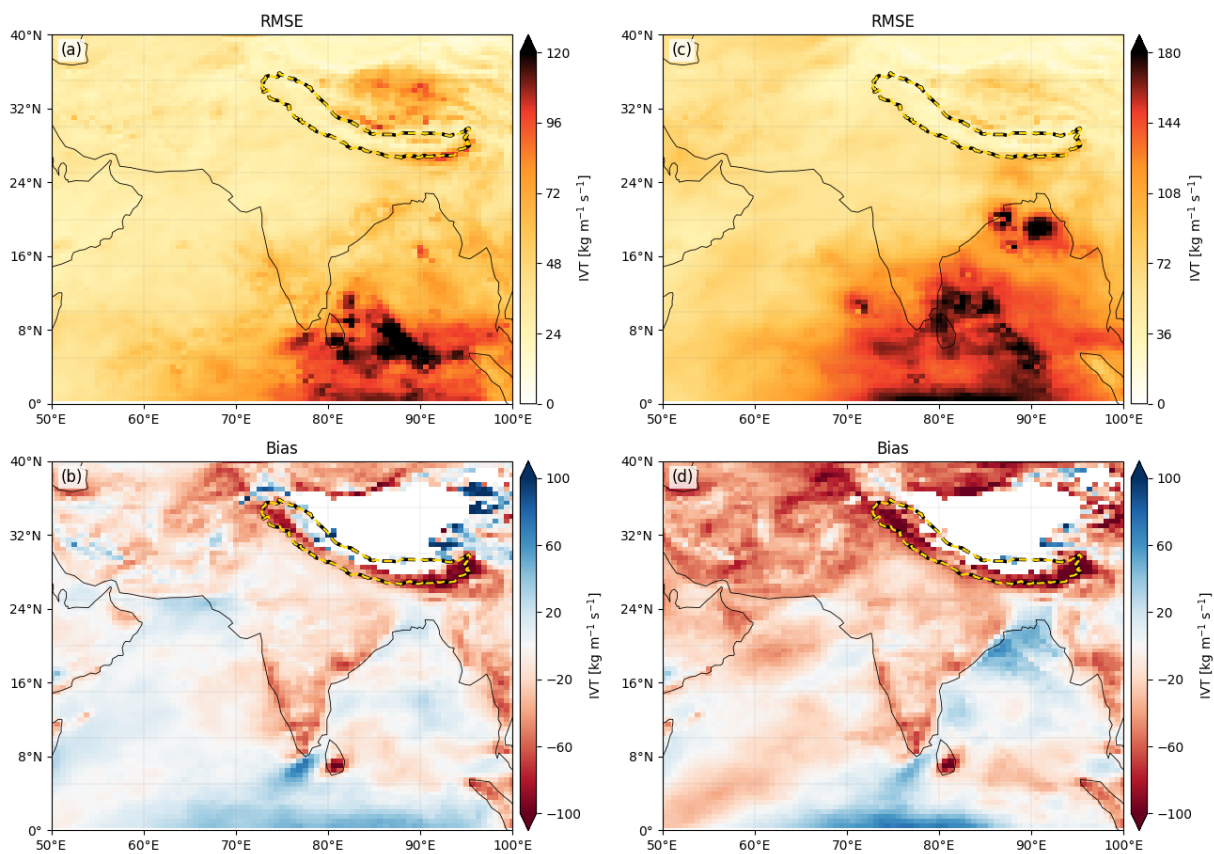
180 The evaluation of the model performance is conducted in a staged approach, beginning with each
181 metric assessment before moving to the validation of atmospheric river (AR) events. In the first
182 stage, the ARcnn magnitude and ARcnn direction models are evaluated as independent CNN
183 models using the statistical metrics previously defined. After the individual performance of these
184 models is established, the combined ARcnn output (magnitude model + direction model) is applied
185 to specific AR events. To detect ARs in the dataset, we leverage the AR detection method
186 developed by Guan and Waliser (2019) and the Kennett (2021). Using this algorithm, first the ARs
187 are detected in the reanalysis test set data, so that we can evaluate the ARcnn AR detection
188 capability on the same dates, and can quantitatively measure the improvement in IVT
189 representation within the boundaries of the ARs. This targeted analysis assesses whether ARcnn
190 effectively captures the intense moisture transport gradients and directional coherence necessary
191 for accurate Himalayan AR forecasting.

192 4.1 ARcnn Magnitude Model Validation

193 For the evaluation of ARcnn postprocessed IVT and GFS model's IVT forecast predictive skills,
194 spatial error maps were plotted for the test set on the domain of analysis. Standard evaluation

195 metrics: Root Mean Square Error (RMSE), Centered Root Mean Square Error (CRMSE), Bias,
196 and Pearson Correlation (PC) were calculated in the form of spatial maps. These maps were
197 utilized to visualize and compare the metrics between GFS and ARcnn models.

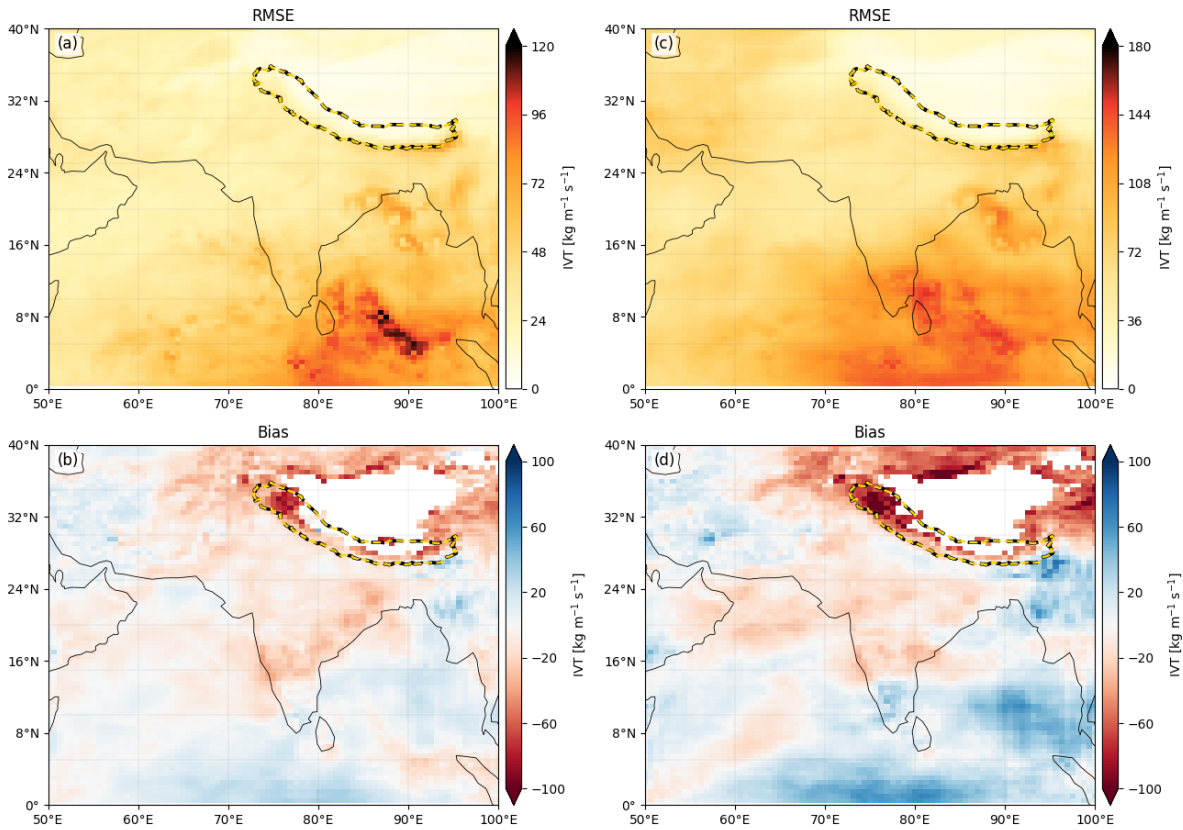
198 In figure 3 the spatial maps show the RMSE and Bias evaluation of GFS IVT with respect to
199 MERRA-2 for 24-hour and 7-day lead forecasts. Bias assessment is restricted to IVT magnitudes
200 $\geq 100 \text{ kg m}^{-1} \text{ s}^{-1}$. This thresholding assures the evaluation remains focused on the high-IVT
201 regimes fundamental for ARs. By screening out low-intensity IVT background noise which display
202 nominal bias shifts or minor degradation, the training prioritizes the core IVT cluster that drive AR
203 body, rather than the peripheral zones where minor IVT errors are trivial. For PC and CRMSE
204 Figure S1 shows the spatial maps for GFS IVT for both 24-hour and 7-day.



205
206 Figure 3. Spatial distribution of RMSE and Bias of IVT GFS IVT forecast. Left panels correspond to 24-hour lead GFS forecasts,
207 while the right panels show results for 7-day lead GFS forecasts. Panels (a) and (c) show RMSE, and panels (b) and (d) show Bias.
208 In the Bias panels, positive values (blue) indicate overestimation and negative values (red) indicate underestimation. The yellow
209 and black dashed boundary represents the Himalayan region.

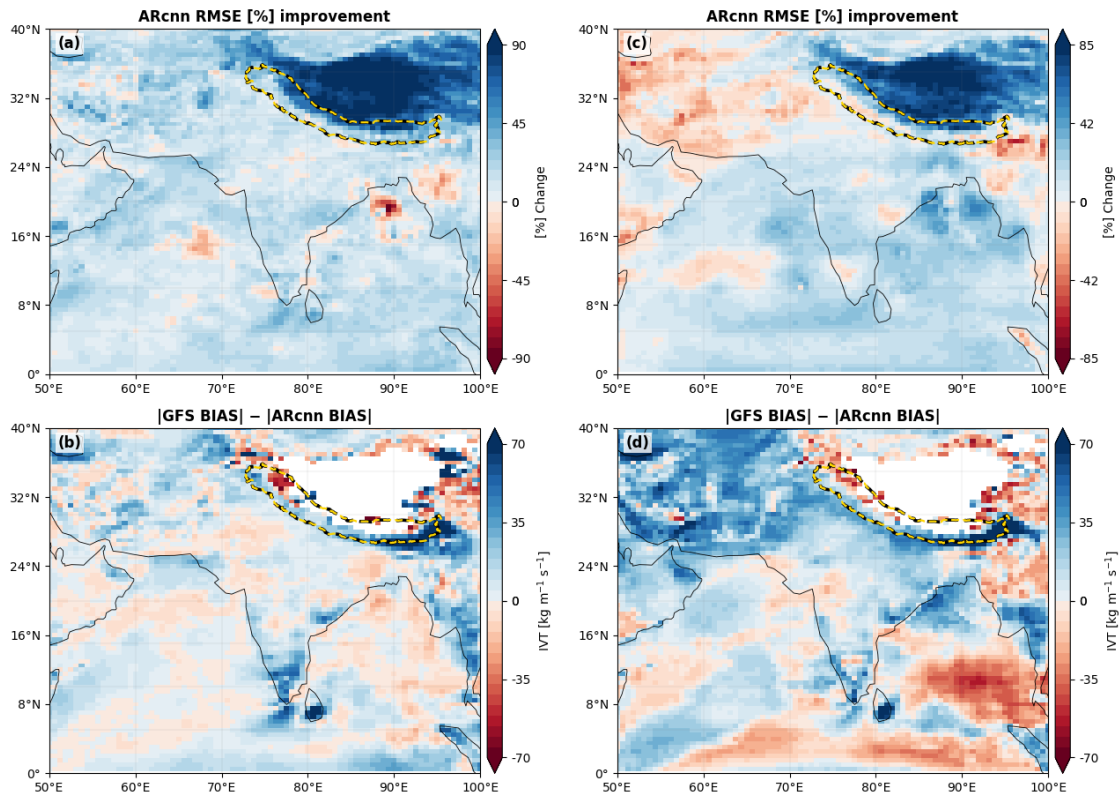
210 The spatial maps of RMSE and bias of postprocessed ARcnn IVT with respect to MERRA-2 IVT
211 for both 24-hour and 7-day lead are shown in Figure 4. Compared to Figure 3, the shift toward

212 lower values signifies a reduction in total error and systematic errors. Similarly in Figure S2 spatial
 213 maps of PC and CRMSE for postprocessed ARcnn IVT also show improvement in the metrics.



214
 215 Figure 4. Spatial distribution of RMSE and Bias for ARcnn postprocessed IVT. Left panels correspond to 24-hour lead ARcnn
 216 forecasts, while the right panels show results for 7-day lead ARcnn forecasts. Panels (a) and (c) show RMSE, and (b) and (d) are
 217 for Bias.

218 Figure 5 shows the RMSE and bias improvement spatial maps of ARcnn postprocessed IVT with
 219 respect to GFS IVT. For the 24-hour and 7-day lead, the full domain averaged RMSE is lowered
 220 by approximately 20.6% and 14.7% respectively. The bias is by 32.7% for the 24-hour lead, and
 221 67.7% for the 7-day lead. In the Himalayan region the RMSE decreases by 41.6% and 21.7% for
 222 the 24-hour and 7-day lead times respectively. Improvement in the CRMSE and PC is shown in
 223 Figure S3 where CRMSE reduces by 17.3% and 18.8% for 20.6% and 14.7% respectively. PC
 224 increases by 5% and 10 % for the 24-hour and 7-day lead respectively. In the Himalayan region
 225 CRMSE is reduced by 30.0% and 17.4% for the 24-hour and 7-day lead respectively, and PC
 226 increases by 22% for both leads.



227

228 Figure 5. Spatial Distribution of Improvement of ARcnn postprocessed IVT with respect to GFS forecasts. Left panels are for 24-
 229 hour lead and right for 7-day lead forecasts. Panels (a) and (c) represent percentage improvement in RMSE, and Panels (b) and (d)
 230 are for absolute bias improvement. The blue colours represent improvement while the red colors indicate degradation.

231 To get the mean improvement in metrics across the entire domain and the Himalayan region, mean
 232 values across the all the spatial metric distribution maps were calculated for both regions as
 233 summarized in Table1.

234

235 Table 1. Domain-averaged IVT magnitude metrics for GFS and ARcnn magnitude model and the corresponding percentage
 236 improvement of ARcnn magnitude model relative to GFS.
 237

Lead Time Region	Metric	GFS	ARcnn	Improvement (%) (ARcnn vs GFS)	
7-day	Himalayan Region	RMSE ($\text{kg m}^{-1} \text{s}^{-1}$)	41.8	32.7	21.7 ↓
		CRMSE ($\text{kg m}^{-1} \text{s}^{-1}$)	36.3	29.9	17.4 ↓
		Bias (IVT ≥ 100)	-72.5	-48.5	33.1 ↓
		Pearson Correlation (PC)	0.40	0.49	21.6 ↑
	Full Domain	RMSE ($\text{kg m}^{-1} \text{s}^{-1}$)	83.5	71.3	14.7 ↓
		CRMSE ($\text{kg m}^{-1} \text{s}^{-1}$)	81.2	65.8	18.8 ↓
		Bias (IVT ≥ 100)	-36.4	-11.7	67.7 ↓
		Pearson Correlation (PC)	0.58	0.65	10.2 ↑
24-hour	Himalayan Region	RMSE ($\text{kg m}^{-1} \text{s}^{-1}$)	34.6	20.2	41.6 ↓
		CRMSE ($\text{kg m}^{-1} \text{s}^{-1}$)	28.2	19.7	30.0 ↓
		Bias (IVT ≥ 100)	-46.5	-34.1	26.9 ↓
		Pearson Correlation (PC)	0.643	0.786	22.2 ↑
	Full Domain	RMSE ($\text{kg m}^{-1} \text{s}^{-1}$)	47.6	37.8	20.6 ↓
		CRMSE ($\text{kg m}^{-1} \text{s}^{-1}$)	44.7	37.1	17.3 ↓
		Bias (IVT ≥ 100)	-17.6	-11.8	32.7 ↓
		Pearson Correlation (PC)	0.85	0.89	4.9 ↑

238

239

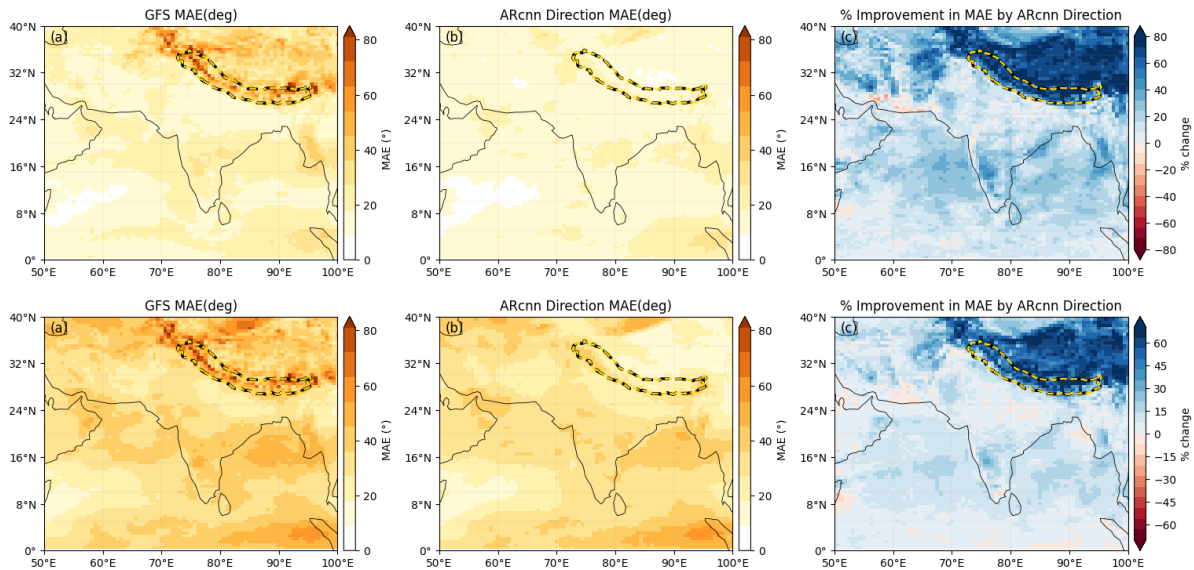
240 4.2 ARcnn Direction Model Validation

241 Since the orientation of AR is a significant component for precipitation associated with it, so the
242 IVT direction improvement is also necessary for better predictability of ARs as well as
243 precipitation (Hecht, C. W. et al.; Griffith HV et al).To evaluate the performance of the ARcnn
244 direction model, the mean angular error (MAE) of the IVT direction is computed at each grid
245 point for both the GFS forecasts and the ARcnn-corrected fields, with respect to MERRA-2, using
246 the independent test dataset. The resulting spatial in maps provide a clear comparison of directional
247 errors across the entire study domain as well as the Himalayan region.

248 Figure 6 is evident to draw the conclusion that the ARcnn direction model achieves a clear
249 reduction in MAE across both the entire domain and the Himalayan region. The improvement is

250 visually apparent from the lower values in Figure 6(b) compared to Figure 6(a), indicating lower
251 directional errors relative to the GFS baseline.

252 Figure 6(c) in both top and bottom rows highlight the widespread improvement, with blue shading
253 prominent in both the Himalayan region and large portions of the full domain, indicating
254 substantial percentage reductions in MAE achieved by the ARcnn model. These results establish
255 the enhanced capability of the ARcnn direction model to correct IVT directional errors, particularly
256 over the complex terrain of the Himalayas.



257
258 Figure 6. Spatial distribution of mean angular error (MAE) in IVT direction for 24-hour (top row) and 7-day (bottom row) lead
259 forecasts. Panels (a) and (b) show MAE for the GFS forecast and the ARcnn direction model, respectively, both evaluated against
260 MERRA-2. In panels (a) and (b), lighter colors indicate smaller directional errors, while darker colors denote larger errors. Panel
261 (c) shows the percentage change in MAE achieved by the ARcnn direction model relative to GFS, where blue colors indicate
262 improvement (error reduction) and red colors indicate degradation. The yellow–black dashed outline marks the Himalayan region.

263 Table 2 briefs the entire region-averaged MAE of IVT direction for the GFS forecast and the
264 ARcnn direction model over both the entire and the Himalayan region for 24-hour and 7-day lead
265 forecasts. The results show that ARcnn consistently outperforms GFS across both lead times. For
266 the 24-hour lead, the mean directional error is reduced by 24.4% over the full domain and by
267 59.2% over the Himalayan region. Likewisw For the 7-day lead forecast, ARcnn reduces the
268 directional error by 15.1% over the full domain and by 44.8% over the Himalayan region. These
269 enhancements establish the improved capability of the ARcnn direction model to correct IVT flow
270 direction, particularly over complex topography such as the Himalayas.

271 Table 2. Region-averaged IVT direction MAE for GFS and ARcnn Direction model, and the corresponding improvement of
 272 ARcnn Direction model over GFS for the full domain and the Himalayan region.

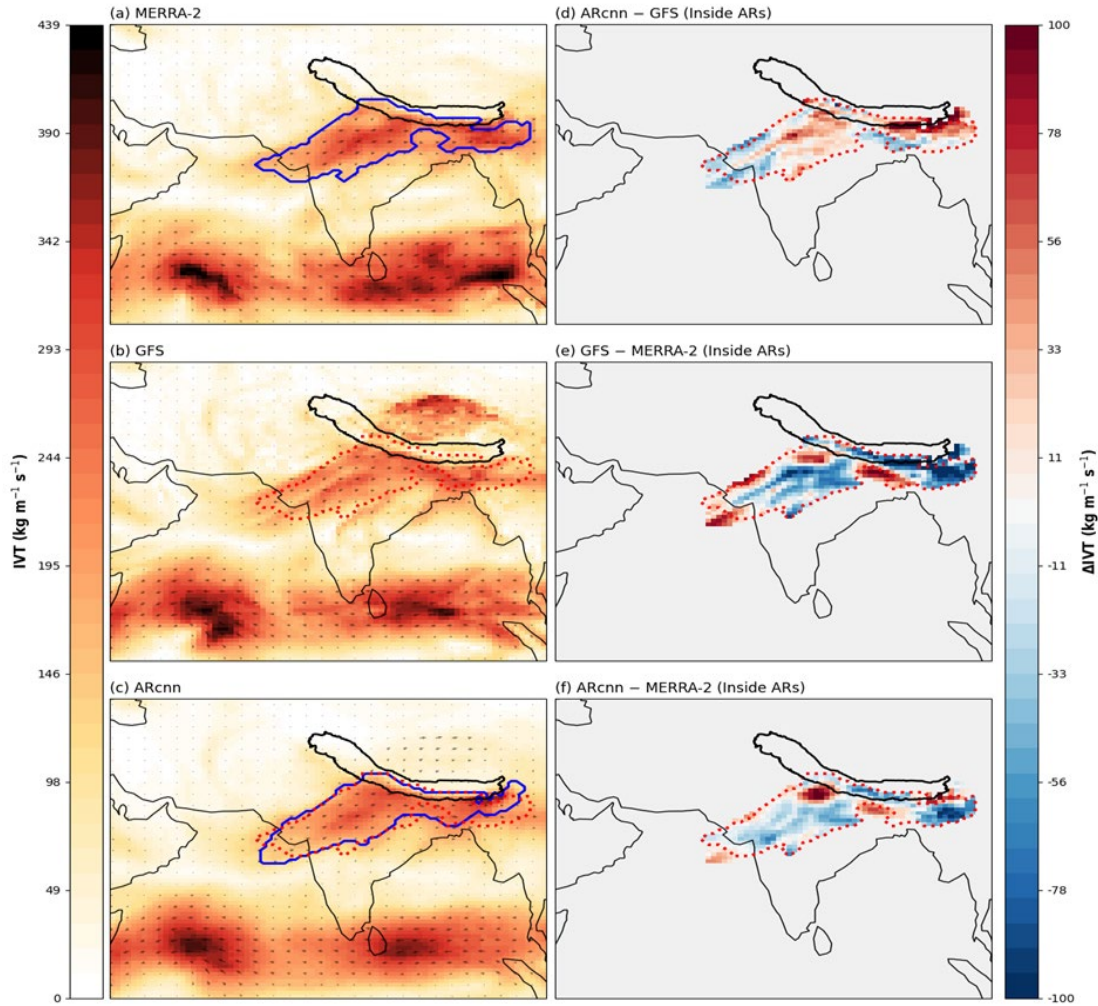
Lead Time	Region	GFS MAE (°)	ARcnn MAE (°)	Absolute Improvement (°)	Percentage Improvement (%)
24-hour	Himalayan	45.1	16.5	28.5	59.2
	Entire	22.2	15.1	7.1	24.4
7-day	Himalayan	51.8	27.2	24.6	44.8
	Entire	36.7	30.4	6.3	15.1

273 4.3 ARcnn Model Performance for AR Events

274 Landfalling Atmospheric River (AR) events in the test dataset are identified using the algorithms
 275 by Guan and Waliser (2019) and the Kennett (2021). A total of three landfalling AR events are
 276 identified during the test period. For these events, quantitative performance metrics, including
 277 RMSE, CRMSE, bias, and Pearson correlation are computed for both the GFS forecasts and the
 278 ARcnn post-processed IVT fields with respect to MERRA-2. This evaluation is used to assess the
 279 improvement achieved by ARcnn specifically during AR conditions. In addition, selected AR case
 280 detected by ARcnn are visually compared with corresponding GFS and MERRA-2 fields to
 281 qualitatively examine improvements in AR structure and intensity.

282 In Figure 7 and Figure 8, AR event for 16 March 2025 has been shown for 24-hour lead and 7-day
 283 lead GFS forecast respectively. In both cases AR is detected the in the ARcnn postprocessed IVT
 284 field which couldn't be detected in the GFS IVT filed. In Figure 6 for 24-hour lead forecast, the
 285 mean GFS IVT forecast is underestimated by 11.6% in the AR field, whereas in the ARcnn
 286 postprocessed IVT filed there is reduced underestimation of 7.0%, this improvement with respect
 287 to the GFS IVT is corresponds to 5.3%. Similarly, for the 7-day GFS lead forecast in Figure 7, the
 288 underestimation by GFS becomes more pronounced, with a mean IVT underestimation of 25.6%.
 289 The ARcnn IVT filed has an underestimation of 20% and delivers an improvement of 7.4% relative
 290 to the GFS forecast.

291 For all the three landfalling Atmospheric River (AR) events identified in the test set, the ARcnn
 292 model demonstrates substantial and consistent improvements over the baseline GFS forecasts
 293 within AR regions, as summarized in Table 3 and Table 4.



294
 295 Figure 7. Atmospheric River (AR) event on 16 March 2025 identified using different models for 24-hour lead time. Panel (a) shows
 296 the MERRA-2 IVT field, blue boundary represents AR detected in MERRA-2, which serves as the reference AR. Panel (b) shows
 297 the GFS IVT forecast, AR was not detected, and the red dotted boundary represents the reference AR. Panel (c) shows that the
 298 ARcnn IVT field, where AR is successfully detected, shown in the blue boundary. Panel (d) displays the IVT difference between
 299 ARcnn and GFS (ARcnn – GFS) within the AR region, highlighting the amount of correction introduced by ARcnn. Panels (e) and
 300 (f) show GFS – MERRA-2 and ARcnn – MERRA-2 IVT differences, respectively. The lighter colors in (f) compared to (e) indicate
 301 reduced IVT errors, confirming that ARcnn improves both IVT magnitude and direction, enabling successful detection of an AR
 302 event missed by GFS. The red dashed line denotes the MERRA-2-detected AR overlaid on all panels, and the black boundary
 303 outlines the Himalayan region.

304 Table3: Metrics for IVT in AR regions in test set for 24-hour lead GFS

Metric	GFS	ARcnn	Change (ARcnn – GFS)
Mean Bias(kg m ⁻¹ s ⁻¹)	-13	-11.3	+1.7(13.2%)
RMSE (kg m ⁻¹ s ⁻¹)	57.5	42.9	↓ 25.3%
CRMSE (kg m ⁻¹ s ⁻¹)	54.8	40.8	↓ 25.6%
Pearson Correlation	0.69	0.83	↑ +0.14(20%)

313

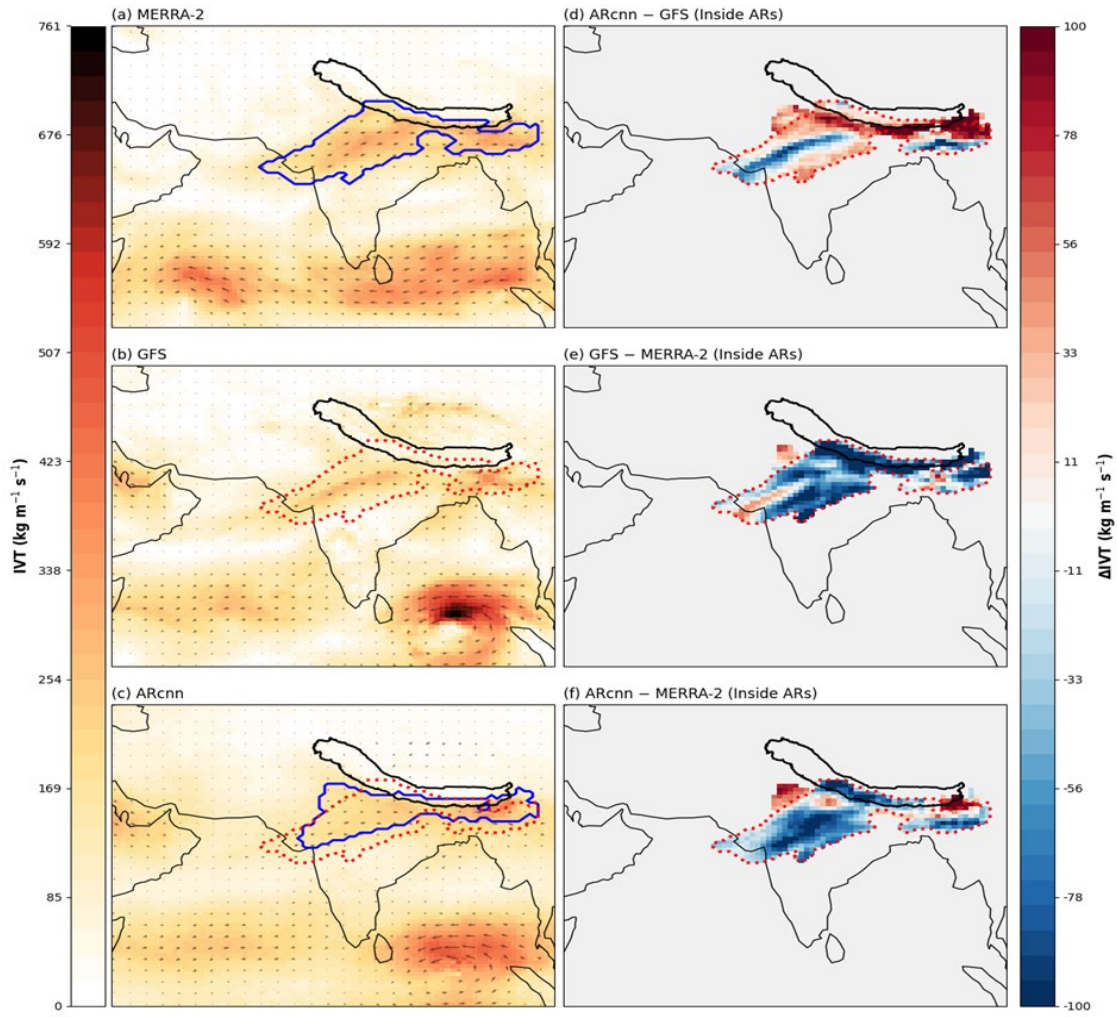


Figure 8. same as Figure 6 for 7-day lead time GFS forecast.

Table 4: Metrics for IVT in AR regions in test set for 7-day lead GFS

Metric	GFS	ARcnn	Change (ARcnn – GFS)
Mean Bias ($\text{kg m}^{-1} \text{s}^{-1}$)	-21.5	-17.1	+4.4 (20.5% improvement)
RMSE ($\text{kg m}^{-1} \text{s}^{-1}$)	87.1	65.8	↓ 24.4%
CRMSE ($\text{kg m}^{-1} \text{s}^{-1}$)	73.8	50.5	↓ 31.5%
Pearson Correlation	0.62	0.75	↑ +0.131 (21.2% improvement)

315

316

317

318

319

320

321

322

323

324

325

326

327 The results discussed in this section show that GFS IVT has degraded performance in the AR zones
328 and also shows that GFS generally underpredicts in these regions. Collectively, these results
329 demonstrate that ARcnn reinforces the moisture transport clusters and improves the depiction of
330 AR intensity and structure across both short-term range (24-hour) and extended (7-day) forecast
331 lead times compared to the baseline GFS forecast.

332 5. Discussion

333 Compared with the improvements in IVT forecast by Chapman et al 2019., who reported an
334 improvement of 9–17% in RMSE and 0.5–12% in PC across 3-hour to 7-day lead times, our model
335 achieves 15-20% and 22-41% improvements in RMSE over the entire domain and the Himalayan
336 region, respectively, and improvements in PC of 5-10% and 20% over the entire and the Himalayan
337 regions, respectively, across 24-hour and 7-day leads. These numbers demonstrate consistent or
338 better improvement over the entire domain, and over the Himalayas, performance is further
339 enhanced. Further, bias metric is the weakest corrected metric in the previous study and stalls after
340 day 5, but our model reduces the bias by about 25-67%.

341 Importantly, direction correction was not incorporated in the previous study, our model corrects
342 the MAE by about 15-24% for entire domain and 45-59% for the Himalayan region. This is
343 extremely important for AR rainfall determination especially in mountainous regions like
344 Himalayas, as the orientation of an AR decides heavy precipitation patterns (Hecht et al. 2017;
345 Griffith et al. 2020). As these results and comparison strongly suggest the improvement of ARcnn
346 in correcting MAE, bias and other metrics, due to this reason the ARcnn was able to correct the
347 IVT of AR, which was not detected in GFS for both 24-hour and 7-day lead.

348 Since the high resolution 0.25° GFS dataset (2015 onwards) is relatively limited for the occurrence
349 of ARs which are not so frequent, this makes the model struggle to reach the best performance.
350 So, if we use hindcasting techniques for generating more forecasts for 100 years and train the
351 model on ARs only which could get better results.

352 The relatively limited availability of high resolution 0.25° GFS dataset (2015 onwards) with
353 respect to the rare occurrences of ARs prevents the model to reach best performance level.
354 Leveraging hindcasting techniques to generate forecasts for 50 years, training the model on ARs
355 only could substantially fetch better outcomes.

356 6. Conclusion

357 The results presented in the research deliver convincing evidence that the convolution neural
358 network model (ARcnn) delivers significant and physically coherent improvements over the
359 baseline GFS IVT forecasts, and thus AR forecasts. By separately correcting IVT magnitude and
360 direction and integrating these components, ARcnn attains systematic error reduction while
361 conserving the spatial structure essential for AR detection for both short term (24-hour) and longer-
362 term (7-day) leads. Importantly, the errors in direction of IVT and ARs observed in GFS forecasts
363 are significantly reduced by the developed convolution neural networks model. An AR's
364 orientation with respect to a topographic barrier is a key factor in resolving the magnitude of
365 precipitation and impacts generated from the AR.

366 Event-based analysis of landfalling ARs shows that ARcnn reinforces moisture transport intensity,
367 reduces AR-region RMSE, CRMSE and significantly improves spatial coherence of IVT. It is
368 illustrated that ARcnn IVT outputs are more suitable for AR identification than the raw GFS
369 forecasts. In general, the ARcnn model is a robust post-processing tool that improves the accuracy
370 and physical realism of IVT forecasts over the Himalayas. The study emphasizes the strong
371 potential of deep learning-based correction algorithms to complement NWP systems for
372 topographically complex and data-sparse regions, with direct consequences for hydrological
373 hazard prediction and early warning systems.

374 7. References

- 375 Bi, K., Xie, L., Zhang, H. et al. Accurate medium-range global weather forecasting with 3D neural
376 networks. *Nature* 619, 533–538 (2023). <https://doi.org/10.1038/s41586-023-06185-3>
- 377 Chapman, W. E., Delle Monache, L., Alessandrini, S., Subramanian, A. C., Ralph, F. M., Xie, S.-P.,
378 Lerch, S., & Hayatbini, N. (2022). Probabilistic predictions from deterministic atmospheric river
379 forecasts with deep learning. *Monthly Weather Review*, 150(1), 215–234.
380 <https://doi.org/10.1175/MWR-D-21-0106>.
- 381 Chapman, W. E., Subramanian, A. C., Delle Monache, L., Xie, S.-P., & Ralph, F. M. (2019).
382 Improving atmospheric river forecasts with machine learning. *Geophysical Research Letters*,
383 46(17–18), 10627–10635. <https://doi.org/10.1029/2019GL083662>
- 384 Chen, L., Zhong, X., Zhang, F. et al. FuXi: a cascade machine learning forecasting system for 15-
385 day global weather forecast. *npj Clim Atmos Sci* 6, 190 (2023). [https://doi.org/10.1038/s41612-](https://doi.org/10.1038/s41612-023-00512-1)
386 [023-00512-1](https://doi.org/10.1038/s41612-023-00512-1)
- 387 Environmental Modeling Center (EMC). (2016). Global Forecast System (GFS) model
388 description. National Centers for Environmental Prediction (NCEP), NOAA.

389 Gelaro, R., McCarty, W., Suárez, M. J., et al. (2017). MERRA-2: Modern-Era Retrospective
390 Analysis for Research and Applications, Version 2. *Journal of Climate*, 30(14), 5419–5454.
391 <https://doi.org/10.1175/JCLI-D-16-0758.1>

392 Gershunov, A., Shulgina, T., Ralph, F. M., Lavers, D. A., & Rutz, J. J. (2017). Assessing the
393 climate-scale variability of atmospheric rivers affecting western North America. *Geophysical*
394 *Research Letters*, 44, 7900–7908. <https://doi.org/10.1002/2017GL074175>

395 Glorot, X., Bordes, A., & Bengio, Y. (2011). Deep sparse rectifier neural networks.
396 <https://proceedings.mlr.press/v15/glorot11a/glorot11a.pdf>

397 Griffith HV, Wade AJ, Lavers DA, Watts G. (2020). Atmospheric river orientation determines flood
398 occurrence. *Hydrological Processes*. 2020;34:4547–4555. <https://doi.org/10.1002/hyp.13905>

399 He, K., Zhang, X., Ren, S., & Sun, J. (2015). Deep residual learning for image recognition. In
400 *Proceedings of the IEEE Conference on Computer Vision and Pattern Recognition (CVPR)*
401 (pp. 770–778). <https://doi.org/10.1109/CVPR.2016.90>

402 Hecht, C. W., and J. M. Cordeira (2017), Characterizing the influence of atmospheric river
403 orientation and intensity on precipitation distributions over North Coastal California, *Geophys.*
404 *Res. Lett.*, 44, 9048–9058, <https://doi.org/10.1002/2017GL074179>

405 Khan, A., Sohail, A., Zahoor, U. et al. A survey of the recent architectures of deep convolutional
406 neural networks. *Artif Intell Rev* 53, 5455–5516 (2020). [https://doi.org/10.1007/s10462-020-](https://doi.org/10.1007/s10462-020-09825-6)
407 [09825-6](https://doi.org/10.1007/s10462-020-09825-6)

408 Lamjiri, M. A., Dettinger, M. D., Ralph, F. M., & Guan, B. (2017). Hourly storm characteristics
409 along the U.S. West Coast: Role of atmospheric rivers in extreme precipitation. *Geophysical*
410 *Research Letters*, 44, 7020–7028. <https://doi.org/10.1002/2017GL074193>

411 Mahto, S. S., Nayak, M. A., Lettenmaier, D. P., & Mishra, V. (2023). Atmospheric rivers that make
412 landfall in India are associated with flooding. *Communications Earth & Environment*, 4, Article
413 135. <https://doi.org/10.1038/s43247-023-00775-9>

414 Nash, D., Carvalho, L. M. V., Rutz, J. J., & Jones, C. (2023). Influence of the freezing level on
415 atmospheric rivers in High Mountain Asia: WRF case studies of orographic precipitation extremes.
416 *Climate Dynamics*, 62, 589–607. <https://doi.org/10.1007/s00382-023-06929-x>

417 Nayak, M. A., Azam, M. F., & Lyngwa, R. V. (2021). ERA5-based database of Atmospheric Rivers
418 over Himalayas. *Earth System Science Data Discussions*. <https://doi.org/10.5194/essd-2020-397>

419 Payne, A.E., Demory, M.-E., Leung, L.R., Ramos, A.M., Shields, C.A., Rutz, J.J., Siler, N.,
420 Villarini, G., Hall, A. and Ralph, F.M., 2020. Responses and impacts of atmospheric rivers to
421 climate change. *Nature Reviews Earth & Environment*, 1, pp.143–157.
422 <https://doi.org/10.1038/s43017-020-0030-5>

423 Ralph, F. M., Rutz, J. J., Cordeira, J. M., Dettinger, M., Anderson, M., Reynolds, D., et al. (2018).
424 A scale to characterize the strength and impacts of atmospheric rivers.
425 <https://doi.org/10.1175/BAMS-D-18-0023.1>

426 Guan, B., Noah P. Molotch, et al. (2010). Extreme snowfall events linked to atmospheric rivers and
427 surface air temperature via satellite measurements. <https://doi.org/10.1029/2010GL044696>

428 ScienceDirect (2024). Sigmoid Function. Available at:
429 <https://www.sciencedirect.com/topics/computer-science/sigmoid-function> [Accessed 24 Oct.
430 2023].

431 Ioffe, S., & Szegedy, C. (2015). Batch normalization: Accelerating deep network training by
432 reducing internal covariate shift. In Proceedings of the 32nd International Conference on Machine
433 Learning (ICML) (pp. 448–456). <https://doi.org/10.48550/arXiv.1502.03167>

434 Shuchang Guo, Yi Yang, Peng Liu Assimilation of the deep learning-corrected global forecast
435 system fields into the regional model for improving medium-range persistent precipitation
436 forecasts <https://doi.org/10.1016/j.atmosres.2024.107318>

437 Yuan, J., Ni, B., & Kassim, A. A. (2014). Half-CNN: A general framework for whole-image
438 regression. National University of Singapore. <https://doi.org/10.48550/arXiv.1412.6885>

439 Singh, S. & Goyal, M. K. An innovative approach to predict atmospheric rivers: Exploring
440 convolutional autoencoder. Atmos. Res. 289, 106754 (2023).
441 <https://doi.org/10.1016/j.atmosres.2023.106754>

442 Tian, Y., Zhao, Y., Son, S.-W., Luo, J.-J., Oh, S.-G., & Wang, Y. (2023). A deep-learning ensemble
443 method to detect atmospheric rivers and its application to projected changes in precipitation
444 regime. Journal of Geophysical Research: Atmospheres, 128, e2022JD037041.
445 <https://doi.org/10.1029/2022JD037041>

446 UCAR Research Data Archive (RDA). (2024). NCEP GFS Global Forecast Grids Historical
447 Archive. University Corporation for Atmospheric Research. <https://rda.ucar.edu>

448 Yu, F., & Koltun, V. (2015). Multi-scale context aggregation by dilated convolutions.
449 <https://doi.org/10.48550/arXiv.1511.07122>

450 Kennett, D. (2021). AR_Detection: Atmospheric River detection algorithm (Version 1.0.0)
451 [Computer software]. GitHub. https://github.com/daemonkennett/ar_detection

452 Guan, B., & Waliser, D. E. (2019). Tracking atmospheric rivers globally: Spatial distributions and
453 temporal evolution of life cycle characteristics. Journal of Geophysical Research: Atmospheres,
454 124(23), 12523–12552. <https://doi.org/10.1029/2019JD031205>

455 Wick, G. A., P. J. Neiman, F. M. Ralph, and T. M. Hamill, 2013: Evaluation of forecasts of the
456 water vapor signature of atmospheric rivers in operational numerical weather prediction models.
457 Weather and Forecasting, 28, 1337–1352. <https://doi.org/10.1175/WAF-D-13-00025.1>

458 Wu, D.-R., Chen, C.-T., & Huang, W.-R. (2026). Characteristics of atmospheric rivers over the
459 Asia–Pacific monsoon region with the modified AR detection algorithm. Journal of the
460 Meteorological Society of Japan, 104, Article 2. <https://doi.org/10.1007/s44394-025-00005-0>

461 Xu, G., Wang, X., Wu, X., Leng, X., & Xu, Y. (2025). Development of skip connection in deep
462 neural networks for computer vision and medical image analysis: A survey.
463 <https://doi.org/10.1016/j.engappai.2024.109890>

464 McCarty, W., Coy, L., Gelaro, R., Huang, A., Merkova, D., Smith, E. B., et al. (2016). MERRA-2
465 input observations: Summary and assessment. Technical Report Series on Global Modeling and
466 Data Assimilation, 46(October). Retrieved from).
467 <https://gmao.gsfc.nasa.gov/pubs/docs/McCarty885.pdf>

468 Zhu, Y., & Newell, R. E. (1998). A proposed algorithm for moisture fluxes from atmospheric
469 rivers. Geophysical Research Letters. [https://doi.org/10.1175/1520-0493\(1998\)126<0725:APAFMF>2.0.CO;2](https://doi.org/10.1175/1520-0493(1998)126<0725:APAFMF>2.0.CO;2)